

Multimillion Atom Simulations of Dynamics of Oxidation of an Aluminum Nanoparticle and Nanoindentation on Ceramics[†]

Priya Vashishta,* Rajiv K. Kalia, and Aiichiro Nakano

Laboratory for Advanced Computing & Simulations, Department of Chemical Engineering & Materials Science, Department of Physics & Astronomy, and Department of Computer Science, University of Southern California, 3651 Watt Way, Los Angeles, California 90089-0242

Received: October 2, 2005; In Final Form: December 20, 2005

We have developed a first-principles-based hierarchical simulation framework, which seamlessly integrates (1) a quantum mechanical description based on the density functional theory (DFT), (2) multilevel molecular dynamics (MD) simulations based on a reactive force field (ReaxFF) that describes chemical reactions and polarization, a nonreactive force field that employs dynamic atomic charges, and an effective force field (EFF), and (3) an atomistically informed continuum model to reach macroscopic length scales. For scalable hierarchical simulations, we have developed parallel linear-scaling algorithms for (1) DFT calculation based on a divide-and-conquer algorithm on adaptive multigrids, (2) chemically reactive MD based on a fast ReaxFF (F-ReaxFF) algorithm, and (3) EFF-MD based on a space–time multiresolution MD (MRMD) algorithm. On 1920 Intel Itanium2 processors, we have demonstrated 1.4 million atom (0.12 trillion grid points) DFT, 0.56 billion atom F-ReaxFF, and 18.9 billion atom MRMD calculations, with parallel efficiency as high as 0.953. Through the use of these algorithms, multimillion atom MD simulations have been performed to study the oxidation of an aluminum nanoparticle. Structural and dynamic correlations in the oxide region are calculated as well as the evolution of charges, surface oxide thickness, diffusivities of atoms, and local stresses. In the microcanonical ensemble, the oxidizing reaction becomes explosive in both molecular and atomic oxygen environments, due to the enormous energy release associated with Al–O bonding. In the canonical ensemble, an amorphous oxide layer of a thickness of ~ 40 Å is formed after 466 ps, in good agreement with experiments. Simulations have been performed to study nanoindentation on crystalline, amorphous, and nanocrystalline silicon nitride and silicon carbide. Simulation on nanocrystalline silicon carbide reveals unusual deformation mechanisms in brittle nanophase materials, due to coexistence of brittle grains and soft amorphous-like grain boundary phases. Simulations predict a crossover from intergranular continuous deformation to intragrain discrete deformation at a critical indentation depth.

1. Introduction

Materials by design efforts have thus far focused on controlling structures at diverse length scales—atoms, defects, fibers, interfaces, grains, pores, etc. Because of the inherent complexity of such multiscale materials phenomena, atomistic simulations are expected to play an important role in the design of materials such as metals, semiconductors, ceramics, and glasses. In recent years we have witnessed rapid progress in large-scale atomistic simulations, highly efficient algorithms for massively parallel machines, and immersive and interactive virtual environments for analyzing and controlling simulations in real time. As a result of these advances, simulation efforts are being directed toward reliably predicting properties of materials in advance of fabrication. Thus, materials simulations are capable of complementing and guiding experimental search for new and novel materials.

Computer simulation is the third mode of scientific research that bridges the gap between analytical theory and laboratory experiment. Experiments search for patterns in complex natural phenomena. Theories encode the discovered patterns into mathematical equations that provide predictive laws for the behavior of nature. Computer simulations solve these equations

numerically in their full complexity, where analytical solutions are prohibitive due to a large number of degrees of freedom, nonlinearity, or lack of symmetry. In computer simulations, environments can be controlled with any desired accuracy and extreme conditions are accessible far beyond the scope of laboratory experiments.

Advanced materials and devices with nanometer grain/feature sizes are being developed to achieve higher strength and toughness in ceramic materials and greater speeds in semiconducting electronic and photonic devices. Below the length scale of 100 nm, however, continuum description of materials and devices must be supplemented by atomistic descriptions.^{1,2} Current state-of-the-art atomistic simulations involve 1 million to 1 billion atoms.³ Finally, the impact of large-scale nanosystem simulations cannot be fully realized without major breakthroughs in scientific visualization. The current practice of sequentially processing visualization data is highly ineffective for large-scale applications that produce terabytes of data. The only viable solution is to integrate visualization into simulation, so that they are both performed concurrently on multiple parallel machines and then examine the results in real time in three-dimensional immersive and interactive virtual environments.⁴

This paper describes our efforts to combine scalable and portable simulation algorithms to enable very large-scale

[†] Part of the special issue “Michael L. Klein Festschrift”.

* Author to whom correspondence should be addressed. E-mail: priyav@usc.edu

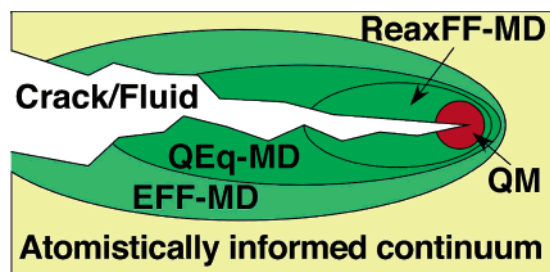


Figure 1. Hierarchical molecular dynamics simulation approach to fracture. Quantum mechanical and ReaxFF-MD computations are performed to study environmental effects on the crack tip. ReaxFF-MD is matched to QEq-MD and to EFF-MD in the process zone. Atomistically informed continuum models are compared with engineering fracture data.

molecular dynamics (MD) simulations. Scalable multiresolution algorithms that enable these large-scale simulations are described in the first part of this paper. In the second part, we discuss the MD simulations of various nanostructured materials and processes of great scientific and technological importance.

2. Hierarchical Simulation Framework

Simulations of material properties and processes require multiple size domains and a different computational approach for each of these domains. In fracture simulations, for example, a quantum mechanical (QM) description is required at the crack tip to take into account the breaking of chemical bonds. One scale up from the electronic level is the atomistic region where understanding of high-rate deformation mechanisms requires atomistic simulations over a region of about 100 nm around the crack tip for about a microsecond. In the vicinity of the crack tip, chemical reactions cause bond breaking and new bond formation over a region of about 10 nm ($\sim 10^5$ atoms). Surrounding this reactive zone is a region of fluctuating atomic charges and defects, which extends to about 50 nm and contains about 10^7 atoms. Outside this region the material is highly deformed and still requires atomistic description up to about 100–200 nm (10^8 – 10^9 atoms). Beyond these length scales, atomistically informed continuum modeling is required.

In simulation studies of fracture, QM methods could be employed around the crack tip where bonds break and non-equilibrium conditions prevail, Figure 1. This region would contain about 10^3 atoms. Atomistic regions near the tip and across interfaces would be studied with a reactive force field (ReaxFF) that Goddard and co-workers have developed on the basis of first-principles calculations to interface QM and effective force field (EFF) methods (Figure 1).⁵ ReaxFF is several orders of magnitude faster than QM methods and can handle much larger systems (10^5 atoms).

In strained regions that do not have active reactions, we use MD based on an EFF with fixed atomic charges. Such an approach is much faster than ReaxFF and can handle up to 10^9 atoms. For example, we have performed a 1.5 billion atom EFF-MD simulation of dynamic fracture in a nanocomposite consisting of SiC fibers in a Si₃N₄ matrix⁶ and a 115 million atom simulation of crack propagation in amorphous silica.^{7,8} Our EFF potentials have been extensively validated against experimental data and QM calculations on cohesive energies, elastic constants, melting temperatures, high-pressure structural transformations, amorphous structures, and fracture energies.

To facilitate smooth transition between ReaxFF and EFF, it is necessary to introduce another computational approach between these methods. Here a nonreactive force field employs

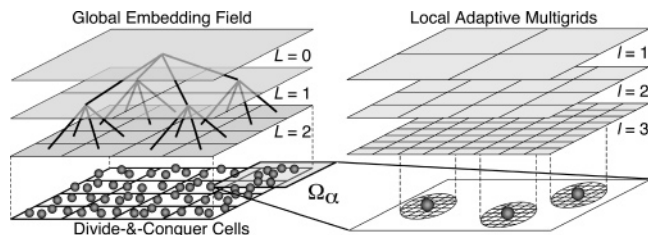


Figure 2. Schematic of an embedded divide-and-conquer (EDC) algorithmic framework. (Left) The physical space is subdivided into spatially localized cells, with local atoms constituting subproblems (bottom), which are embedded in a global field (shaded) solved with a tree-based algorithm. (Right) To solve the subproblem in domain Ω_α in the EDC-DFT algorithm, coarse multigrids (gray) are used to accelerate iterative solutions on the original real-space grid (corresponding to the grid refinement level, $l = 3$). The bottom panel shows that fine grids are adaptively generated near the atoms (spheres) to accurately operate the ionic pseudopotentials on the electronic wave functions.

geometry-dependent charges, based on the charge equilibration (QEq) method.^{9–12}

We have designed a framework not only to integrate QM and ReaxFF/QEq/EFF-MD methods automatically but also to allow a coarse-grained simulation to dynamically invoke multiple fine-grained simulations.¹³ This framework consists of (1) a hierarchical division of the physical system into subsystems of increasing quality-of-solution (QoS) requirements, $S_0 \supset S_1 \supset \dots \supset S_n$, and (2) a suite of simulation services, M_α ($\alpha = 0, 1, \dots, n$), of ascending order of accuracy (e.g., EFF < QEq < ReaxFF < QM). We have used the additive hybridization framework to perform (1) QM/EFF-MD simulations of crack initiation in Si in the presence of water molecules,¹⁴ (2) EFF-MD/finite element (FE) simulations of stress distributions at Si/amorphous Si₃N₄ interfaces,¹⁵ and (3) QM/EFF-MD/FE simulations of oxidation in Si.¹³

3. Parallel Linear-Scaling Atomistic Simulation Algorithms

To perform the large-scale hierarchical simulations described in the previous section, it is essential that each simulation method covers sufficiently wide length scales, and this in turn requires scalable simulation algorithms on massively parallel computers. We have developed a unified algorithmic framework to design linear-scaling algorithms for broad scientific and engineering problems, based on data locality principles. In the embedded divide-and-conquer (EDC) algorithms, spatially localized subproblems are solved in a global embedding field, which is efficiently computed with tree-based algorithms (Figure 2). Examples of the embedding field are the electrostatic field in molecular dynamics (MD) simulations, the self-consistent Kohn–Sham potential in the density functional theory (DFT),¹⁶ and a coarser simulation in a multiscale simulation.

Specifically, we have developed a suite of linear-scaling MD simulation algorithms for materials simulations, in which interatomic forces are computed with increasing accuracy and complexity. The linear-scaling algorithms encompass a wide spectrum of physical reality: (1) classical MD based on a many-body interatomic potential model, which involves the formally $O(N^2)$ N -body problem, (2) environment-dependent, ReaxFF-MD, which involves the $O(N^3)$ variable N -charge problem, and (3) QM calculation based on the DFT, to provide approximate solutions to the exponentially complex quantum N -body problem.

We have developed chemically reactive $O(N)$ MD simulation algorithms, on the basis of our space–time multiresolution

molecular dynamics (MRMD) algorithm.³ In the MD approach, one obtains the phase-space trajectories of the system (positions and velocities of all atoms at all times). Atomic force laws for describing how atoms interact with each other are mathematically encoded in the interatomic potential energy, $E_{\text{MD}}(\mathbf{r}^N)$, which is a function of the positions of all N atoms, $\mathbf{r}^N = \{\mathbf{r}_1, \mathbf{r}_2, \dots, \mathbf{r}_N\}$, in the system. In our many-body interatomic potential scheme, $E_{\text{MD}}(\mathbf{r}^N)$ is expressed as an analytic function that depends on relative positions of atomic pairs and triplets. Time evolution of \mathbf{r}^N is governed by a set of coupled ordinary differential equations. For interatomic potentials with finite ranges, the computational cost is made $O(N)$ using a linked-list cell approach. For the long-range electrostatic interaction, we use the fast multipole method (FMM) to reduce the $O(N^2)$ computational complexity of the N -body problem to $O(N)$.^{17–19} In the FMM, the physical system is recursively divided into subsystems to form an octree data structure, and the electrostatic field is computed recursively on the octree with $O(N)$ operations, while maintaining the spatial locality at each recursion level. Our scalable parallel implementation of the FMM has a unique feature to compute atomistic stress tensor components, based on a novel complex charge method.¹⁹ The MRMD algorithm also utilizes temporal locality through multiple time stepping (MTS), which uses different force-update schedules for different force components.^{18,20} Specifically, forces from the nearest-neighbor atoms are computed at every MD step, whereas forces from farther atoms are updated less frequently.

For parallelization of MD simulations, we use spatial decomposition.³ The total volume of the system is divided into P subsystems of equal volume, and each subsystem is assigned to a node in an array of P compute nodes. To calculate the force on an atom in a subsystem, the coordinates of the atoms in the boundaries of neighbor subsystems are “cached” from the corresponding nodes. After updating the atomic positions due to a time-stepping procedure, some atoms may have moved out of its subsystem. These atoms are “migrated” to the proper neighbor nodes. With the spatial decomposition, the computation scales as N/P , while communication scales in proportion to $(N/P)^{2/3}$ for an N -atom system. Tree-based algorithms such as the FMM incur an $O(\log P)$ overhead, which is negligible for coarse-grained ($N/P > 10^4$) applications.

Physical realism of MD simulations is greatly enhanced by incorporating variable atomic charges and reactive bond orders, which dynamically adapt to the local environment. However, the increased realism of this ReaxFF-MD⁵ is accompanied by increased computational complexity, $O(N^3)$, for solving a dense linear system of equations to determine atomic charges at every MD step, i.e., the variable N -charge problem. We have developed a scalable fast reactive force-field (F-ReaxFF) MD algorithm, which reduces the complexity to $O(N)$ by combining the FMM based on spatial locality and an iterative minimization approach to utilize the temporal locality of the solutions. To further accelerate the convergence, we use a multilevel preconditioned conjugate-gradient (MPCG) method, by splitting the Coulomb-interaction matrix into short- and long-range components and using the sparse short-range matrix as a preconditioner.²¹ The extensive use of the sparse preconditioner enhances the data locality and thereby improves the parallel efficiency.

The chemical bond order, B_{ij} , is an attribute of an atomic pair, (i, j) , and changes dynamically depending on the local environment. In ReaxFF, the interatomic potential energies between atomic pairs, triplets, and quartets depend on the bond orders of all constituent atomic pairs. Force calculations in ReaxFF MD thus include up to atomic 4-tuples explicitly, and

require information on 6-tuples implicitly due to chain-rule differentiations through the bond orders. To efficiently handle the resulting multiple interaction ranges, the F-ReaxFF employs a multilayer cellular decomposition (MCD) scheme for caching atomic n -tuple ($n = 2-6$) information.

An atom consists of a nucleus and surrounding electrons, and quantum mechanics explicitly treats the electronic degrees of freedom. The DFT reduces the exponentially complex quantum N -body problem to a self-consistent matrix eigenvalue problem, which can be solved with $O(M^3)$ operations (M is the number of independent electronic wave functions and is on the order of N).¹⁶ The DFT can be formulated as a minimization of the energy functional, $E_{\text{QM}}(\mathbf{r}^N, \psi^M)$, with respect to electronic wave functions, $\psi^M(\mathbf{r}) = \{\psi_1(\mathbf{r}), \psi_2(\mathbf{r}), \dots, \psi_M(\mathbf{r})\}$, subject to orthonormality constraints.

For scalable quantum-mechanical calculations, linear-scaling DFT algorithms are essential.²² We have previously developed an $O(M)$ DFT algorithm based on unconstrained minimization of a modified energy functional and a localized-basis approximation.²³ Recently, we have designed a new $O(M)$ DFT algorithm with considerably more robust convergence properties, controlled errors, and energy conservation during MD simulations.²⁴ The divide-and-conquer DFT algorithm represents the physical system as a union of overlapping spatial domains, $\Omega = \cup_{\alpha} \Omega_{\alpha}$ (Figure 2),²⁵ and physical properties are computed as linear combinations of domain properties. For example, the electronic density is expressed as $\rho(\mathbf{r}) = \sum_{\alpha} p^{\alpha}(\mathbf{r}) \sum_n f_n^{\alpha} |\psi_n^{\alpha}(\mathbf{r})|^2$, where $p^{\alpha}(\mathbf{r})$ is a support function that vanishes outside the α th domain Ω_{α} , and f_n^{α} and $\psi_n^{\alpha}(\mathbf{r})$ are the occupation number and the wave function of the n th electronic state (i.e., Kohn–Sham orbital) in Ω_{α} . The domains are embedded in a global Kohn–Sham potential, which is a functional of $\rho(\mathbf{r})$ and is determined self-consistently with $\{f_n^{\alpha}, \psi_n^{\alpha}(\mathbf{r})\}$. We use the multigrid method to compute the global potential.

The DFT calculation in each domain is performed using a real-space approach,²⁶ in which electronic wave functions are numerically represented on grid points, Figure 2. The real-space grid is augmented with coarser multigrids to accelerate the convergence of iterative solutions.^{27,28} Furthermore, a finer grid is adaptively generated near every atom, to accurately operate ionic pseudopotentials to describe electron–ion interactions. We include electron–ion interactions using norm-conserving pseudopotentials²⁹ and the exchange–correlation energy in a generalized gradient approximation.³⁰

The divide-and-conquer DFT algorithm on the hierarchical real-space grids is implemented on parallel computers based on spatial decomposition. Each compute node contains one or more domains of the EDC algorithm. For each domain, its electronic structure is computed independently, with little information needed from other compute nodes (only the global density but not individual wave functions is communicated). The resulting large computation/communication ratio makes this approach highly scalable on parallel computers.

The convergence of the new algorithm has been verified for nontrivial problems such as amorphous CdSe and liquid Rb.²⁴ The divide-and-conquer DFT calculation for alumina (with the domain size $9.0 \times 7.8 \times 8.2 \text{ au}^3$ and the buffer lengths 4.5, 3.9, and 4.1 au) reproduces an $O(N^3)$ DFT energy within 0.001 au per atom. The EDC-DFT MD algorithm has also overcome the energy drift problem, which plagues most $O(N)$ DFT-based MD algorithms.

We have also developed a framework to map the above $O(N)$ algorithms onto massively parallel computers with deep memory hierarchies. This framework maximally exposes data locality

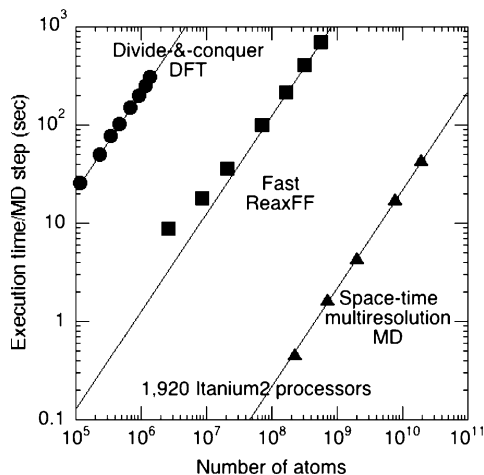


Figure 3. Benchmark tests of reactive and nonreactive MD simulations on 1920 Itanium2 processors of Columbia. The figure shows the total execution time per MD step as a function of the number of atoms for three linear-scaling algorithms: quantum-mechanical MD based on the divide-and-conquer density functional theory (circles); fast reactive force-field MD (squares); and space–time multiresolution MD (triangles). Lines show ideal $O(N)$ scaling.

and exploits parallelism at multiple decomposition levels. The parallelization framework includes a topology-preserving computational spatial decomposition scheme to minimize latency through structured message passing and load imbalance/communication costs through a novel wavelet-based load-balancing scheme.³¹

The three parallel MD algorithms—MRMD, F-ReaxFF, and divide-and-conquer DFT—are portable and have been run on various platforms, including Intel Itanium2, Intel Xeon, AMD Opteron, and IBM Power4 based parallel computers. For example, scalability tests of the three parallel algorithms have been performed on the 10 240-processor Columbia supercomputer at the NASA Ames Research Center, Figure 3. The 64-bit Itanium2 architecture operates at 1.5GHz and is capable of issuing two multiply–add operations per cycle for a peak performance of 6 Gflop/s. Columbia is configured as a cluster of 20 Altix boxes, each with 512 processors and approximately 1 TB of global shared-access memory.

Major design parameters for MD simulations of materials include the number of atoms in the simulated system and the methods to compute interatomic forces (classically in MRMD, semiempirically in F-ReaxFF MD, or quantum-mechanically in DFT MD). Figure 3 shows a design-space diagram for classical and quantum-mechanical MD simulations on 1920 Itanium2 processors of Columbia. The largest benchmark tests in this study include 18 925 056 000 atom MRMD, 557 383 680 atom F-ReaxFF, and 1 382 400 atom (121 385 779 200 electronic degrees of freedom) divide-and-conquer DFT calculations. The figure demonstrates perfect linear scaling for all the three algorithms, with prefactors spanning five orders of magnitude. The only exception is the F-ReaxFF algorithm below 100 million atoms, where the execution time scales even sublinearly. This is due to the decreasing communication overhead, which scales as $O((N/P)^{-1/3})$. Our algorithmic and parallel-computing frameworks expose maximal data locality, and as a result the parallel efficiency on 1920 processors is as high as 0.953.

4. Oxidation of an Aluminum Nanoparticle

Oxidation plays a critical role in the performance and durability of various nanosystems. Oxidation of metallic nanoparticles offers an interesting possibility of synthesizing nano-

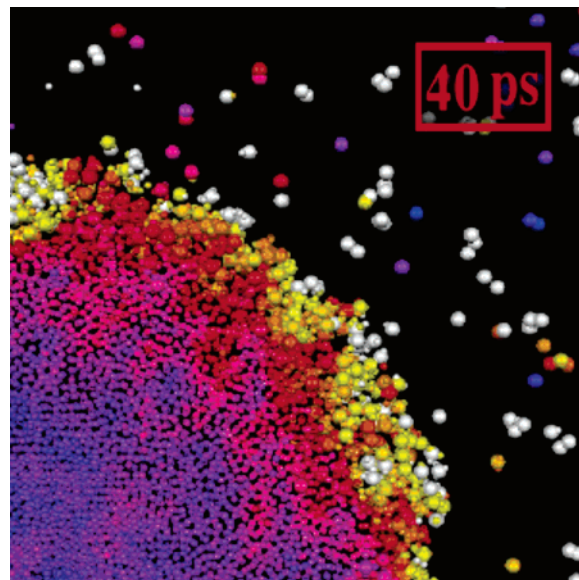


Figure 4. Temperature of atoms during the microcanonical MD simulation of an Al nanoparticle in an oxygen environment. The larger spheres correspond to oxygen, and smaller spheres to aluminum; color represents the temperature

composites with both metallic and ceramic properties. We have performed the first successful MD simulation of oxidation of an Al nanoparticle (diameter 200 Å).^{11,12} The MD simulations are based on the interaction scheme developed by Streitz and Mintmire, which can successfully describe a wide range of physical properties of both metallic and ceramic systems.¹⁰ This scheme is capable of treating bond formation and bond breakage and changes in charge transfer as the atoms move and their local environments are altered. The QEq-MD simulations are performed in both microcanonical and canonical ensembles.

In the microcanonical simulation, energy released from Al–O bond formation is rapidly transported into the nanocluster resulting in disordering of the Al nanocrystal and outward expansion of the oxide region (Figure 4). The thickness of the oxide region increases linearly with time and does not saturate. By 50 ps the thickness and temperature of the oxide region are 35 Å and 2500 K, respectively. Subsequently, numerous small Al_xO_y fragments are ejected from the nanocluster surface, indicating that the nanocluster is exploding. This behavior under closed conditions has also been observed experimentally.

The canonical simulations provide detailed picture of the rapid evolution and culmination of the surface oxide thickness, local stresses, and atomic diffusivities. In the first 5 ps, oxygen molecules dissociate and the oxygen atoms first diffuse into octahedral and subsequently into tetrahedral sites in the Al nanoparticle. In the next 20 ps, as the oxygen atoms diffuse radially into and the Al atoms diffuse radially out of the nanoparticle, the fraction of 6-fold coordinated oxygen atoms drops dramatically. Concurrently, there is a significant increase in the number of O atoms, forming clusters of corner-sharing and edge-sharing OAl_4 tetrahedra. Between 30 and 35 ps, clusters of OAl_4 coalesce to form a neutral, percolating tetrahedral network that impedes further intrusion of oxygen atoms into and of Al atoms out of the nanoparticle. At 50 ps the diffusivities of aluminum and oxygen are 1.4×10^{-4} and 1.1×10^{-4} cm²/s, respectively. The local pressure after 100 ps of simulation time in Figure 5 shows that the oxide layer is predominantly tensile, which may have a significant implication for the mechanical stability of a passivated Al nanoparticle. The electrostatic and nonelectrostatic contributions to the local

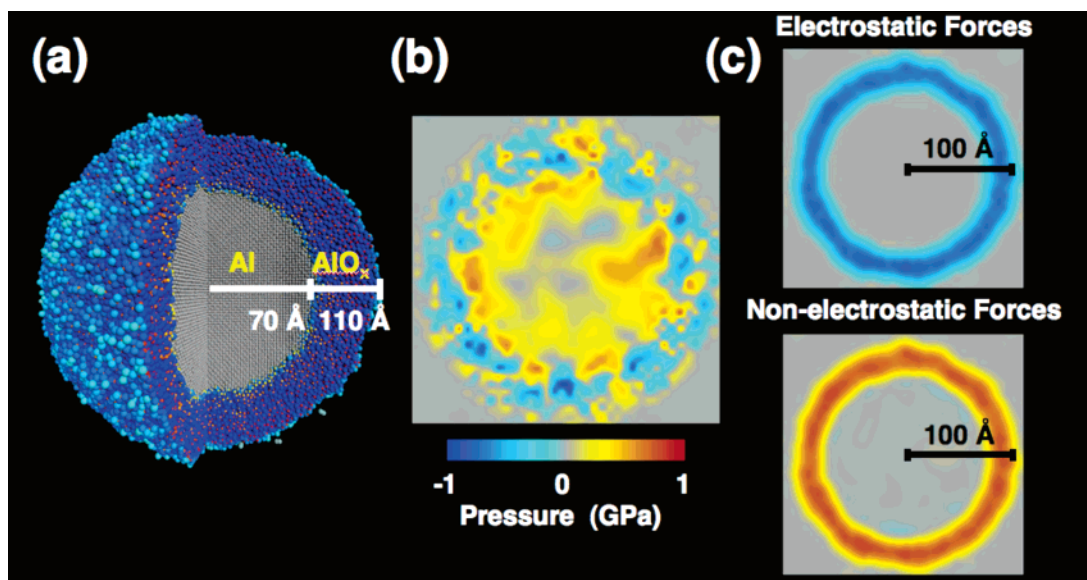


Figure 5. (a) Snapshot of the Al nanocluster after 0.5 ns of canonical MD simulation time. (A quarter of the system is cut out to show the aluminum/aluminum oxide interface.) The larger spheres correspond to oxygen, and smaller spheres to aluminum; color represents the charge on an atom. (b) Local pressure in the nanocluster after 100 ps of simulation time. (c) Electrostatic and nonelectrostatic contributions to the local pressure in Figure 5b.

pressure in the nanocluster are also shown in Figure 5, and they indicate that the attractive electrostatic interaction between Al and O ions is responsible for the tension in the oxide layer. A stable oxide scale formed at the end of our simulation is shown in Figure 5. Structural analysis reveals a 40-Å-thick amorphous oxide scale on the Al nanoparticle. The thickness and structure of the oxide scale are in accordance with experimental results.³² The MD simulations provide a detailed picture of the rapid evolution and culmination of the surface oxide thickness, local stresses, and atomic diffusivities. Clusters of OAl₄ coalesce to form a neutral, percolating tetrahedral network that impedes further intrusion of oxygen atoms into and of Al atoms out of the nanoparticle.

5. Nanoindentation on Ceramics

Nanoindentation testing is a unique local probe of mechanical properties of materials and used extensively to assess the reliability and durability of structural components. The importance of atomistic-level understanding of the nanoindentation process is widely recognized.

We have performed multimillion atom MD simulations of nanoindentation in crystalline and amorphous silicon nitride, using a diamond-shaped indenter, Figure 6.^{33,34} The simulations reveal local amorphization under the indenter. Nanocracks under the indenter corners or material pileup along the indenter edges tends to arrest amorphization. The calculated value of hardness for crystalline Si₃N₄ is in reasonable agreement with experimental results. The predicted hardness value of amorphous Si₃N₄ was later confirmed by nanoindentation experiments.³⁵

We have also performed indentation simulations of 3C crystalline,^{36,37} amorphous,³⁸ and nanocrystalline³⁹ silicon carbide, using a square-based indenter. The load-displacement response of 3C crystal shows an elastic shoulder followed by a plastic regime consisting of a series of load drops, Figure 7a. Analyses of bond angles, local pressure and shear stress, and shortest-path rings show that these drops are related to dislocation activities under the indenter. We show that amorphization is driven by coalescence of dislocation loops and that there is a strong correlation between load-displacement response and ring distribution.

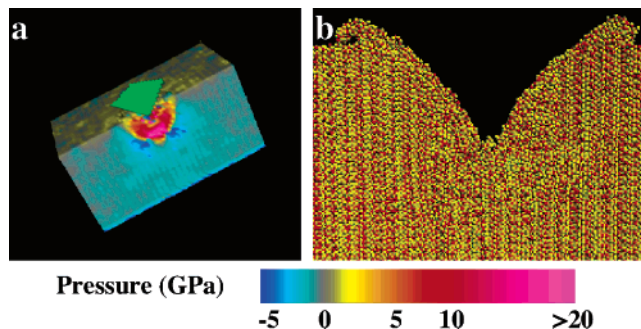


Figure 6. (a) Half-slice view of pressure in a silicon nitride sample during nanoindentation. (b) Atomic view showing amorphization under the indenter and material pileup at the edges of the indenter. Red and yellow are silicon and nitrogen atoms, respectively. These figures demonstrate the relationship between residual stresses and atomistic-level amorphization phenomena.

The load-displacement curve of amorphous SiC also exhibits a series of load drops, reflecting the short-range topological order similar to crystalline 3C-SiC, Figure 7b. In contrast to 3C-SiC, however, the load drops are irregularly spaced and less pronounced. The damage is spatially more extended than in 3C-SiC, and it exhibits long-range oscillations consistent with the indenter size. Hardness is ~60% lower than in 3C-SiC and is in agreement with experiment. The onset of plastic deformation occurs at depth ~75% lower than in 3C-SiC.

The great interest in nanostructured ceramics originates from unique mechanical properties observed or expected in these materials. Examples include very high hardness as well as high fracture toughness and superplastic behavior in normally brittle ceramics. Silicon carbide is of particular interest due to its potential technological applications in high-temperature structural and electronic components. Recent experiments of nanoindentation of nanocrystalline SiC (n-SiC) films with grain sizes of 5–20 nm have shown “superhardness”, i.e., hardness largely exceeding that of a bulk crystalline SiC (3C-SiC).⁴⁰ The experimental hardness was shown to be sensitive to the grain size and the fraction of the amorphous giga byte (GB) phase; however their effects on mechanical responses at the atomistic level are largely unknown.

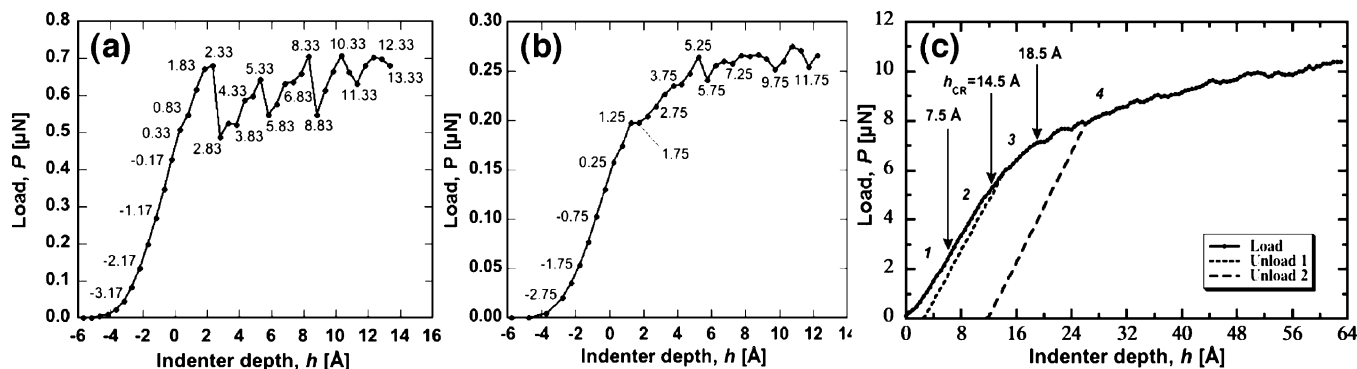


Figure 7. Load–displacement curve during indentation of (a) crystalline, (b) amorphous, and (c) nanocrystalline silicon carbide.

The indentation simulations of n-SiC consisted of a $625 \times 625 \times 625 \text{ \AA}^3$ n-SiC substrate, with randomly oriented grains of an average diameter of 8 nm, containing 18.7 million atoms, with a density of 2.97 g/cm^3 at a temperature 300 K.³⁹ The resulting P – h curve is shown in Figure 7c (solid line), together with two unloading curves (dashed lines). The P – h response exhibits four characteristic regimes. Regime 1 is entirely elastic and ends at $h = 7.5 \text{ \AA}$. Regime 2 extends up to the crossover depth $h_{\text{CR}} \approx 14.5 \text{ \AA}$ and is characterized by a very small hysteresis during unloading as compared to a much more pronounced plastic yield at h_{CR} . Because up to h_{CR} the amorphous “cementlike” GBs hold the grains together, Regimes 1 and 2 are characterized by cooperative continuous intergranular response. Regime 3 starts when amorphous GBs yield plastically at $h_{\text{CR}} \approx 14.5 \text{ \AA}$, and henceforth grains are effectively decoupled from one another. The crystalline phase within the grains does not yield until the onset of regime 4 at $h = 18.5 \text{ \AA}$. Discrete plastic events, such as a dislocation glide, take place within the grains in close proximity to the indenter and are reflected in the rougher character of the P – h curve. Similar periodic load drops have been observed for the nanoindentation in bulk 3C–SiC, Figure 7a. In the case of n-SiC, the load drops are much less pronounced than in 3C–SiC, because the calculated load is averaged over a few grains covered by the indenter and the discrete events in a grain are decoupled from those in the neighboring grains. Our estimate of n-SiC hardness (defined as maximum load divided by the cross-sectional area of the indenter) of 39 GPa is in excellent agreement with the experimental value of “superhardness” of 30–50 GPa for grain sizes of 5–20 nm.⁴⁰

Essential ingredients of predictive MD simulations are reliable interatomic potentials. For example, we have developed an interatomic potential for SiC and validated it by comparing a number of physical quantities with experimental data. The potential parameters are chosen to reproduce the lattice constant, elastic constants, and cohesive energy of 3C–SiC crystal. Good agreements between MD and experimental (or DFT) results are obtained for (1) high-pressure structural transformation in crystalline SiC including both forward and reverse transformations,⁴¹ (2) the phonon density of states of crystalline 3C–SiC, (3) the sintering temperature of nanophase SiC,⁴² (4) amorphous structure, (5) the unstable stacking fault energy for the (111) glide plane in the $[10\bar{1}]$ direction,⁴³ and (6) anisotropic fracture toughness values of 3C–SiC.⁴³

For the 3C-to-rocksalt structural transformation of SiC, we have proposed a new transition mechanism based on MD simulations,⁴¹ which was later confirmed by DFT calculations.⁴⁴ We have also investigated the structure and mechanical behavior of n-SiC by a joint large-scale MD/neutron-scattering experiment study.⁴² In both experiment and simulation, the onset of sintering

is around 1500 K. The effect of consolidation on mechanical properties is also investigated with the MD approach. The results show a power-law dependence of elastic moduli on the density with an exponent of 3.4 ± 0.1 . Details of the interatomic potential for SiC are published elsewhere.⁴⁵

6. Discussion

Current multi-teraflop parallel supercomputers (operating trillions of floating-point operations per second) enable large-scale MD simulations involving up to a billion atoms. Petaflop computers (operating 10^{15} floating-point operations per second) anticipated to be built in the next 5–10 years are expected to enable trillion atom MD simulations.

In the same time frame, metacomputing on a grid of geographically distributed supercomputers, mass storage, and a virtual environment connected via high-speed networks will revolutionize computational research by enabling (1) very large-scale computations that are beyond the power of a single supercomputer and (2) collaborative, hybrid computations that integrate distributed, multiple expertise. A multidisciplinary application that will soon require grid-level computing is emerging at the forefront of computational science and engineering. We have recently developed such a multiscale simulation approach that seamlessly combines continuum mechanics based on the FE method, MD simulations to describe atomistic processes, and QM calculations based on the DFT to handle breakage and formation of atomic bonds.

These emerging new computer architectures, together with further developments in scalable simulation algorithms and parallel-computing frameworks, will be critical for the advancement of modeling and simulation research. Some of the most exciting and challenging opportunities in simulation research lie at the nano–bio interface.

Acknowledgment. This work was partially supported by the AFOSR-DURINT, ARO-MURI, DARPA-PROM, DOE, and NSF. Benchmark tests were performed using the NASA Columbia supercomputers at the NASA Ames Research Center and at the Department of Defense’s Major Shared Resource Centers under a DoD Challenge Project. The simulations described in this paper were carried out in collaboration with our past and current graduate research assistants, postdoctoral research associates, and our long-term overseas collaborators, in particular, with Professor Gurcan Aral, Dr. Rupak Biswas, Dr. Tomothy J. Campbell, Dr. Adri van Duin, Professor William A. Goddard III, Dr. Eleftherios Lidorikis, Professor Shuji Ogata, Professor Fuyuki Shimojo, Dr. Deepak Srivastava, and Professor Izabela Szlufarska.

References and Notes

- (1) Broughton, J. Q.; Abraham, F. F.; Bernstein, N.; Kaxiras, E. *Phys. Rev. B* **1999**, *60*, 2391.
- (2) Nakano, A.; Bachlechner, M. E.; Kalia, R. K.; Lidorikis, E.; Vashishta, P.; Voyiadjis, G. Z.; Campbell, T. J.; Ogata, S.; Shimojo, F. *Comput. Sci. Eng.* **2001**, *3* (4), 56.
- (3) Nakano, A.; Kalia, R. K.; Vashishta, P.; Campbell, T. J.; Ogata, S.; Shimojo, F.; Saini, S. *Scientific Programming* **2002**, *10*, 263.
- (4) Sharma, A.; Nakano, A.; Kalia, R. K.; Vashishta, P.; Kodiyalam, S.; Miller, P.; Zhao, W.; Liu, X. L.; Campbell, T. J.; Haas, A. *Presence: Teleoperators and Virtual Environments* **2003**, *12*, 85.
- (5) van Duin, A. C. T.; Dasgupta, S.; Lorant, F.; Goddard, W. A. *J. Phys. Chem. A* **2001**, *105*, 9396.
- (6) Vashishta, P.; Nakano, A. *Comput. Sci. Eng.* **1999**, *1*, 20.
- (7) Kalia, R. K.; Nakano, A.; Vashishta, P.; Rountree, C. L.; Van Brutzel, L.; Ogata, S. *Int. J. Fract.* **2003**, *121*, 71.
- (8) Lu, Z.; Nomura, K.; Sharma, A.; Wang, W.; Zhang, C.; Nakano, A.; Kalia, R. K.; Vashishta, P.; Bouchaud, E.; Rountree, C. *Phys. Rev. Lett.* **2005**, *95*, 135501.
- (9) Rappe, A. K.; Goddard, W. A. *J. Phys. Chem.* **1991**, *95*, 3358.
- (10) Streit, F. H.; Mintmire, J. W. *Phys. Rev. B* **1994**, *50*, 11996.
- (11) Campbell, T.; Kalia, R. K.; Nakano, A.; Vashishta, P.; Ogata, S.; Rodgers, S. *Phys. Rev. Lett.* **1999**, *82*, 4866.
- (12) Campbell, T. J.; Aral, G.; Ogata, S.; Kalia, R. K.; Nakano, A.; Vashishta, P. *Phys. Rev. B* **2005**, *71*.
- (13) Ogata, S.; Lidorikis, E.; Shimojo, F.; Nakano, A.; Vashishta, P.; Kalia, R. K. *Comput. Phys. Commun.* **2001**, *138*, 143.
- (14) Ogata, S.; Shimojo, F.; Kalia, R. K.; Nakano, A.; Vashishta, P. *J. Appl. Phys.* **2004**, *95*, 5316.
- (15) Lidorikis, E.; Bachlechner, M. E.; Kalia, R. K.; Nakano, A.; Vashishta, P.; Voyiadjis, G. Z. *Phys. Rev. Lett.* **2001**, *87*, 086104.
- (16) Hohenberg, P.; Kohn, W. *Phys. Rev.* **1964**, *136*, B864.
- (17) Greengard, L.; Rokhlin, V. *J. Comput. Phys.* **1987**, *73*, 325.
- (18) Nakano, A.; Kalia, R. K.; Vashishta, P. *Comput. Phys. Commun.* **1994**, *83*, 197.
- (19) Ogata, S.; Campbell, T. J.; Kalia, R. K.; Nakano, A.; Vashishta, P.; Vemparala, S. *Comput. Phys. Commun.* **2003**, *153*, 445.
- (20) Martyna, G. J.; Tuckerman, M. E.; Tobias, D. J.; Klein, M. L. *J. Chem. Phys.* **1994**, *101*, 4177.
- (21) Nakano, A. *Comput. Phys. Commun.* **1997**, *104*, 59.
- (22) Goedecker, S. *Rev. Mod. Phys.* **1999**, *71*, 1085.
- (23) Shimojo, F.; Kalia, R. K.; Nakano, A.; Vashishta, P. *Comput. Phys. Commun.* **2001**, *140*, 303.
- (24) Shimojo, F.; Kalia, R. K.; Nakano, A.; Vashishta, P. *Comput. Phys. Commun.* **2005**, *167*, 151.
- (25) Yang, W. *Phys. Rev. Lett.* **1991**, *66*, 1438.
- (26) Chelikowsky, J. R.; Saad, Y.; Ögüt, S.; Vasiliev, I.; Stathopoulos, A. *Phys. Status Solidi B* **2000**, *217*, 173.
- (27) Fattebert, J.-L.; Bernholc, J. *Phys. Rev. B* **2000**, *62*, 1713.
- (28) Beck, T. L. *Rev. Mod. Phys.* **2000**, *72*, 1041.
- (29) Troullier, N.; Martins, J. L. *Phys. Rev. B* **1991**, *43*, 8861.
- (30) Perdew, J. P.; Burke, K.; Ernzerhof, M. *Phys. Rev. Lett.* **1996**, *77*, 3865.
- (31) Nakano, A. *Concurrency: Practice and Experience* **1999**, *11*, 343.
- (32) Sanchez-Lopez, J. C.; Fernandez, A.; Conde, C. F.; Conde, A.; Morant, C.; Sanz, J. M. *Nanostruct. Mater.* **1996**, *7*, 813.
- (33) Walsh, P.; Kalia, R. K.; Nakano, A.; Vashishta, P.; Saini, S. *Appl. Phys. Lett.* **2000**, *77*, 4332.
- (34) Walsh, P.; Omeltchenko, A.; Kalia, R. K.; Nakano, A.; Vashishta, P.; Saini, S. *Appl. Phys. Lett.* **2003**, *82*, 118.
- (35) Vila, M.; Caceres, D.; Prieto, C. *J. Appl. Phys.* **2003**, *94*, 7868.
- (36) Szlufarska, I.; Kalia, R. K.; Nakano, A.; Vashishta, P. *Appl. Phys. Lett.* **2004**, *85*, 378.
- (37) Szlufarska, I.; Kalia, R. K.; Nakano, A.; Vashishta, P. *Phys. Rev. B* **2005**, *71*.
- (38) Szlufarska, I.; Kalia, R. K.; Nakano, A.; Vashishta, P. *Appl. Phys. Lett.* **2005**, *86*.
- (39) Szlufarska, I.; Nakano, A.; Vashishta, P. *Science* **2005**, *309*, 911.
- (40) Liao, F.; Girshick, S. L.; Mook, W. M.; Gerberich, W. W.; Zachariah, M. R. *Appl. Phys. Lett.* **2005**, *86*.
- (41) Shimojo, F.; Ebbsjo, I.; Kalia, R. K.; Nakano, A.; Rino, J. P.; Vashishta, P. *Phys. Rev. Lett.* **2000**, *84*, 3338.
- (42) Chatterjee, A.; Kalia, R. K.; Nakano, A.; Omeltchenko, A.; Tsuruta, K.; Vashishta, P.; Loong, C. K.; Winterer, M.; Klein, S. *Appl. Phys. Lett.* **2000**, *77*, 1132.
- (43) Kikuchi, H.; Nakano, A.; Kalia, R. K.; Vashishta, P.; Branicio, P. S.; Shimojo, F. *J. Appl. Phys.* **2005**, *98*, 103524.
- (44) Catti, M. *Phys. Rev. Lett.* **2001**, *87*, 035504.
- (45) Vashishta, P.; Kalia, R. K.; Nakano, A.; Rino, J. P. *Phys. Rev. B*, to be published.